

Numerical Simulation of Spin-Dependent Recombination and Hyperfine Structure in Electrically-Detected Magnetic Resonance of 4H–SiC

Deval M. Deliwala,¹ Ryan Byrne,² and Daniel R. Hart^{3,4}

¹⁾*Department of Mathematics, University of California, Berkeley, Berkeley, California 94720, USA*

²⁾*School of Applied and Engineering Physics, Cornell University, Ithaca, New York 14850, USA*

³⁾*Optics and Photonics Branch, NASA Glenn Research Center, Cleveland, Ohio 44135, USA*

⁴⁾*Department of Physics and Mathematics, Southern University and A&M College, Baton Rouge, Louisiana 70813, USA*

(*Electronic mail: daniel.hart@sus.edu)

(Dated: 8 January 2026)

We model continuous-wave Electrically-Detected Magnetic Resonance (EDMR) spectra associated with the negatively charged silicon vacancy (V_{Si}^-) center in 4H–SiC using an effective defect-carrier pair model, and validate the simulation against experimental measurements. The steady-state Liouville framework incorporates Zeeman, hyperfine, zero-field splitting, and exchange interactions to reproduce the measured current contrast as a function of magnetic field. The simulation accurately captures the dominant resonance structure and predicts additional weak features adjacent to the primary transitions. Within the model these secondary resonances arise from hyperfine-assisted transitions and appear as off-resonant sidebands of the main electron-spin resonance, providing testable predictions for future frequency-swept EDMR measurements.

I. INTRODUCTION

Sensitive detection of magnetic resonance in semiconductors plays a central role in both applied sensing technologies and the characterization of spin-dependent transport processes. Electrically detected magnetic resonance (EDMR) is a particularly powerful technique in this context, as it probes spin dynamics indirectly through changes in electrical conductivity arising from spin-dependent recombination (SDR). Because the electrical signal reflects recombination kinetics rather than direct spin polarization, EDMR can exhibit sensitivities that exceed those of conventional electron paramagnetic resonance (EPR), while remaining compatible with device-scale semiconductor platforms.^{1,3}

In wide-bandgap semiconductors, EDMR has attracted renewed interest due to the emergence of point defects with long spin lifetimes and strong coupling to charge transport. Among these materials, silicon carbide (SiC) is especially attractive owing to its low intrinsic spin-orbit coupling, reduced magnetic noise environment, and technological maturity in electronic and optoelectronic device fabrication.^{4,5} In particular, the negatively charged silicon vacancy (V_{Si}^-) center in 4H-SiC has been extensively studied using optical and optically detected magnetic resonance (ODMR) techniques, which establish a quartet ground state with a pronounced axial zero-field splitting and hyperfine coupling to nearby ^{29}Si and ^{13}C nuclei.^{5,6} These same spin properties also make V_{Si}^- an active participant in spin-dependent recombination processes detectable via EDMR.^{3,7}

While EDMR spectra of SiC defects have been reported experimentally, quantitative interpretation remains challenging due to the interplay of coherent spin dynamics, hyperfine interactions, electron-electron coupling, and non-equilibrium recombination kinetics.^{3,8–10} In contrast to ODMR, where fluorescence provides a rel-

atively direct measure of spin populations, the EDMR signal depends sensitively on how microwave-driven spin mixing modulates the balance between singlet and triplet recombination pathways.^{10–12} As a result, modeling EDMR requires a unified treatment of spin Hamiltonian dynamics and irreversible population transfer processes. Effective pair models, in which a localized defect spin interacts with a nearby carrier spin, have proven useful in capturing the essential physics of SDR, but their application to realistic multi-level systems with hyperfine structure and driven dynamics remains an active area of development.^{3,9}

In this work, we present a numerical simulation framework for continuous-wave EDMR spectra associated with the V_{Si}^- center in 4H-SiC, based on an effective defect-carrier pair model. By treating the defect ground state as a spin-1/2 doublet, we represent the system as a minimal two-electron, two-nuclear-spin manifold that retains the spin degrees of freedom relevant to recombination while remaining computationally tractable. Coherent dynamics arising from Zeeman, hyperfine, dipolar, and exchange interactions are combined with singlet-selective recombination and dissociation processes within a steady-state stochastic Liouville formalism. Microwave excitation is incorporated through a rotating-wave approximation, allowing direct simulation of field-swept cw-EDMR spectra without explicit time propagation.^{8,9}

By fitting the simulated spectra to experimental cw-EDMR measurements, we show that this framework accurately reproduces the dominant resonance features of the V_{Si}^- system and captures weaker structures arising from hyperfine-assisted and dipolar-mediated transitions. The model further predicts off-resonant sidebands and half-field features whose dependence on transverse dipolar coupling provides insight into the underlying spin-spin interactions. These results demonstrate that steady-state Liouville simulations offer a quantitative and physically

transparent approach for interpreting EDMR spectra in SiC and related defect-based semiconductor systems and provide testable predictions for future frequency-resolved EDMR experiments.^{8–11}

II. MODEL

We model cw-EDMR using a spin-dependent recombination (SDR) pair consisting of V_{Si}^- and a conduction-band electron. Optical and ODMR studies show that the V_{Si}^- ground state in 4H-SiC is a quartet ($S = 3/2$) with an approximately axial zero-field splitting on the order of tens of MHz.^{13–15} Here we restrict attention to a single Kramers doublet of this manifold and represent it by an effective spin-1/2, which is sufficient to reproduce the cw-EDMR spectra analyzed below. This reduction places the V_{Si}^- -carrier complex in the standard coupled spin-1/2 pair framework widely used in spin-dependent recombination and EDMR modeling.^{16–19}

We treat the pair as two electron spins $S_1 = S_2 = 1/2$ coupled to two nearby nuclei: one ^{29}Si and one ^{13}C , each with $I = 1/2$. Within this framework, the total spin Hamiltonian \mathcal{H} is

$$\mathcal{H} = \mathcal{H}_Z + \mathcal{H}_{HF} + \mathcal{H}_{ZFS} + \mathcal{H}_{EX}, \quad (1)$$

where \mathcal{H}_Z denotes Zeeman interactions of electron and nuclear spins, \mathcal{H}_{HF} the hyperfine coupling to nearby nuclei, \mathcal{H}_{ZFS} the inter-electron dipolar (spin–spin) interaction that produces an *effective* triplet zero-field splitting upon projection, and \mathcal{H}_{EX} the isotropic exchange between defect and carrier spins. This 16-level model is sufficient to reproduce the measured cw-EDMR features analyzed below.

The composite Hilbert space for the two-electron + two-nuclei system is

$$\mathcal{H} = \left(\frac{1}{2}\text{-electron}\right)^{\otimes 2} \otimes \left(\frac{1}{2}\text{-nucleus}\right)^{\otimes 2}, \quad \dim \mathcal{H} = 16.$$

We represent \mathcal{H} in the basis $\mathcal{B} = \{|S, M_S\rangle \otimes |m_{I_1}\rangle |m_{I_2}\rangle\}$, i.e. a coupled-electron basis and a nuclear Zeeman basis. The relevant sub-Hamiltonians are

$$\begin{aligned} \mathcal{H}_Z &= \mu_B \mathbf{B}_0 \cdot (g_1 \mathbf{S}_1 + g_2 \mathbf{S}_2) \\ &\quad + \mu_N \mathbf{B}_0 \cdot (g_{n,\text{Si}} \mathbf{I}_{\text{Si}} + g_{n,\text{C}} \mathbf{I}_{\text{C}}), \\ \mathcal{H}_{HF} &= \mathbf{S}_1 \cdot \mathbf{A}_{a1} \cdot \mathbf{I}_{\text{Si}} + \mathbf{S}_2 \cdot \mathbf{A}_{b1} \cdot \mathbf{I}_{\text{Si}} \\ &\quad + \mathbf{S}_1 \cdot \mathbf{A}_{a2} \cdot \mathbf{I}_{\text{C}} + \mathbf{S}_2 \cdot \mathbf{A}_{b2} \cdot \mathbf{I}_{\text{C}}, \\ \mathcal{H}_{ZFS} &= \mathbf{S}_1 \cdot \mathbf{D} \cdot \mathbf{S}_2, \\ \mathcal{H}_{EX} &= J \mathbf{S}_1 \cdot \mathbf{S}_2, \end{aligned}$$

where $\mathbf{S}_{1,2}$ are the electron spin vector operators for defect and carrier, respectively, $\mathbf{I}_{\text{Si/C}}$ are nuclear spin operators, $\mathbf{A}_{a1}, \mathbf{A}_{b1}, \mathbf{A}_{a2}, \mathbf{A}_{b2}$ are hyperfine tensors coupling each nucleus to each electron spin, \mathbf{D} is the traceless dipolar tensor describing the effective magnetic dipole–dipole coupling within the defect-carrier pair, and J is the scalar

isotropic exchange. Here nucleus “1” denotes a nearby ^{29}Si and nucleus “2” denotes a nearby ^{13}C , each with $I = 1/2$. The four hyperfine tensors $\mathbf{A}_{a1}, \mathbf{A}_{b1}, \mathbf{A}_{a2}, \mathbf{A}_{b2}$ allow each nucleus to couple separately to the defect electron (\mathbf{S}_1 , labeled “a”) and to the carrier electron (\mathbf{S}_2 , labeled “b”). This preserves a two-electron/two-nucleus Hilbert space with $\dim \mathcal{H} = 16$ while allowing distinct contact couplings on the two electronic spins. For the calculations below we take all hyperfine couplings to be isotropic contact terms, $\mathbf{A}_{a1} = A_{a1} \mathbb{1}$, $\mathbf{A}_{b1} = A_{b1} \mathbb{1}$, $\mathbf{A}_{a2} = A_{a2} \mathbb{1}$, and $\mathbf{A}_{b2} = A_{b2} \mathbb{1}$, and take \mathbf{D} to be an effective axial dipolar tensor parameterized by axial D_1 and transverse D_2 . The total electron spin is given by $\mathbf{S} = \mathbf{S}_1 + \mathbf{S}_2$.

1. Stochastic Liouville Equation

A modified Stochastic Liouville Equation (SLE)²⁰,

$$\frac{d\rho}{dt} = -\frac{i}{\hbar} [\mathcal{H}, \rho] - \frac{1}{2} (k_S + k_D) \{\Lambda_S, \rho\} - \frac{1}{2} k_D \{\Lambda_T, \rho\} + \frac{p}{16} \mathbb{1}$$

describes coherent dynamics and dissipative population loss/creation for the defect-carrier pair. Singlet pairs leave the ensemble via recombination at rate k_S in addition to dissociation at k_D ; triplets dissociate at k_D . Here $\Lambda_S = |S\rangle\langle S| \otimes \mathbb{1}_{\text{nuc}}$ and $\Lambda_T = \sum_{m=-1}^1 |T_m\rangle\langle T_m| \otimes \mathbb{1}_{\text{nuc}}$ are projectors on the two-electron sector (tensored with the nuclear identity), and the uniform source term $p/16$ injects carriers at rate p .

In continuous-wave EDMR, microwaves and bias voltages are applied continuously. On nanosecond–microsecond timescales the spin system approaches a balance among driven transitions, relaxation, and recombination/capture, while the measured current is averaged over ms. The steady-state condition is imposed,

$$\frac{d\rho_{ss}}{dt} = 0. \quad (2)$$

Spin-selection rules make recombination predominantly singlet-selective; thus the EDMR signal is modeled as proportional to the steady-state singlet population,

$$I(B_0) = I_0 + A \text{Tr}(\Lambda_S \rho_{ss}), \quad (3)$$

with A and I_0 phenomenological scaling/offset constants. Because the experimental observable is the lock-in derivative $\partial I / \partial B_0$, the offset I_0 cancels identically and the proportionality constant A acts only as an overall amplitude normalization of the simulated derivative spectrum; we therefore absorb A into the fit normalization and do not report it as a physical parameter.

2. Solving for steady-state

Equation 2 can be written as a continuous-time Sylvester equation of Lyapunov type,

$$\mathcal{L}\rho_{ss} + \rho_{ss}\mathcal{L}^\dagger = -Q, \quad (4)$$

where

$$\mathcal{L} = -\frac{i}{\hbar}\mathcal{H} - \frac{1}{2}(k_S + k_D)\Lambda_S - \frac{1}{2}k_D\Lambda_T, \quad Q = \frac{p}{16} \mathbb{1}_{16 \times 16}.$$

For computation we solve Eq. (4) directly as a Sylvester equation of the form $AX + XB = C$ using `scipy.linalg.solve_sylvester`²¹. This is algebraically equivalent to the vectorized 256×256 linear system obtained from $\text{vec}(\mathcal{L}\rho + \rho\mathcal{L}^\dagger)$. The resulting ρ_{ss} is the solution of Equation 2 determined by \mathcal{H} and the kinetic parameters (k_S, k_D, p) . Consequently, varying B_0 at fixed $(A_{a1}, A_{b1}, A_{a2}, A_{b2}, D, J, k_S, k_D, p)$ produces $\rho_{ss}(B_0)$ and consequently $I(B_0)$ from Equation 3. In this formulation ρ_{ss} is not normalized to unit trace; instead $\text{Tr } \rho_{ss}$ reflects the steady-state population of the defect-carrier pair, set by the balance between injection p and the loss rates k_S and k_D .

3. Rotating-Wave Approximation

In EDMR experiments, a continuous microwave drive is also applied to induce magnetic-dipole transitions between the spin sublevels of the defect-carrier pair and create resonances. This microwave excitation is introduced through a time-dependent Zeeman term

$$\mathcal{H}_1 = \mu_B \mathbf{B}_1 \cos(\omega t) \cdot (g_1 \mathbf{S}_1 + g_2 \mathbf{S}_2),$$

where \mathbf{B}_1 is the oscillating field and ω the drive frequency. We transform to the frame rotating at ω about \hat{z} using $U(t) = \exp[-i\omega t(S_{1z} + S_{2z})]$, which yields $\tilde{\mathcal{H}} = U^\dagger(\mathcal{H} + \mathcal{H}_1)U - \hbar\omega(S_{1z} + S_{2z})$. For $g_1 \simeq g_2$ the dominant electron Zeeman splitting is $\omega_0 \approx g_e\mu_B B_0/\hbar$, and resonance occurs when $\omega \approx \omega_0$. In the near-resonant, weak-coupling regime $\omega_0 \gg \omega_1, |J|/\hbar, |A|/\hbar, |D|/\hbar$, counter-rotating terms oscillating near $2\omega_0$ average out. Neglecting them gives the rotating-wave approximation (RWA), under which the Hamiltonian becomes time-independent:

$$\mathcal{H}_{\text{RWA}} = \mathcal{H} - \hbar\omega(S_{1z} + S_{2z}) + \frac{\hbar\omega_1}{2}(S_{1x} + S_{2x}), \quad (5)$$

where, assuming $g_1 \simeq g_2 \simeq g_e$, $\omega_1 = g_e\mu_B B_{1,\perp}/\hbar$ is the Rabi frequency determined by the transverse component of \mathbf{B}_1 . The resulting level splittings depend on the detuning $\Delta = \omega_0 - \omega$, while the transverse term drives the spin flips responsible for resonant transitions. This time-independent form captures the essential driven spin dynamics without explicit time-propagation. \mathcal{H}_{RWA} consequently replaces \mathcal{H} when solving Equation 2. The microwave-driven steady state $\rho_{ss}(B_0, \omega)$ is obtained. Sweeping over B_0 at a fixed microwave drive ω produces the simulated EDMR spectrum.

4. Eigen-energy Simulations

Eigen-energies of the coupled electron-nuclear system are simulated to visualize the field-dependent structure of

the spin ensemble and to identify points where singlet and triplet states become nearly degenerate. Such crossings enhance singlet-triplet mixing, facilitating resonant SDR transitions. The calculation also provides a framework for examining how individual sub-Hamiltonians influence the appearance and strength of these degeneracies, which give rise to observable features in EDMR spectra.

Figure 1 shows the eigen-energy structure of the coupled spin system under the static Hamiltonian \mathcal{H} and the effective RWA Hamiltonian \mathcal{H}_{RWA} , evaluated using the best-fit parameter set in Table II at $\nu = 200$ MHz. In the static case, the triplet manifold exhibits the expected Zeeman-like splitting with B_0 , while singlet states vary weakly with B_0 . Their vertical energy offsets arise from the exchange and ZFS terms, which separate the singlet from the triplet manifold even at $B_0 = 0$. As B_0 increases, several triplet branches cross the flat singlet levels, producing degeneracies that cause singlet-triplet mixing driving SDR. Small asymmetries about $B_0 = 0$ arise from the unequal hyperfine couplings of the silicon and carbon nuclei, which slightly distort the otherwise symmetric Zeeman pattern.

When the system is transformed under the RWA, the drive frequency shifts the energy reference such that resonances occur when $B_{\text{res}} = h\nu/(g_e\mu_B) \approx 71.4$ G. Around these fields, the triplet branches are brought into resonance with the drive, and the same singlet-triplet crossings seen in the static picture align at B_{res} . These crossings indicate where microwave excitation most effectively mixes spin states, enabling SDR at the resonances. Thus, the RWA spectrum provides a direct visualization of the energy structure at play under an EDMR sweep.

5. Parameter estimation and least-squares fitting

The free parameters comprise the effective spin Hamiltonian ($J, A_{a1}, A_{b1}, A_{a2}, A_{b2}, D, g$ factors), the kinetic rates (k_S, k_D, p), and instrumental quantities (drive frequency and Rabi frequency; the overall amplitude in Eq. (3) is absorbed into normalization). Initial values were chosen near reported EPR/ODMR/ENDOR parameters for V_{Si}^- in 4H-SiC and its nearby ^{29}Si and ^{13}C ligands, together with microsecond-scale SDR rates and MHz-scale exchange/dipolar couplings typical of SDR pair models.^{13,22–25} Physical constants (h, \hbar, μ_B, μ_N) were fixed at CODATA values. The prior set and bounds are summarized in Table I.

For a given parameter vector θ , the simulation evaluates the steady-state current $I(B_0; \theta)$ on a uniformly spaced internal field grid $B_j \in [B_{\min}, B_{\max}]$ with N_{int} points. At each B_j the steady-state density matrix $\rho_{ss}(B_j)$ is obtained by solving the Lyapunov equation (4) using the Liouvillian constructed from the driven Hamiltonian \mathcal{H}_{RWA} in Eq. (5). The EDMR current $I(B_j)$ is then computed from Eq. (3).

The experiment measures the first-harmonic lock-in derivative signal $\partial I / \partial B_0$ under sinusoidal field modula-

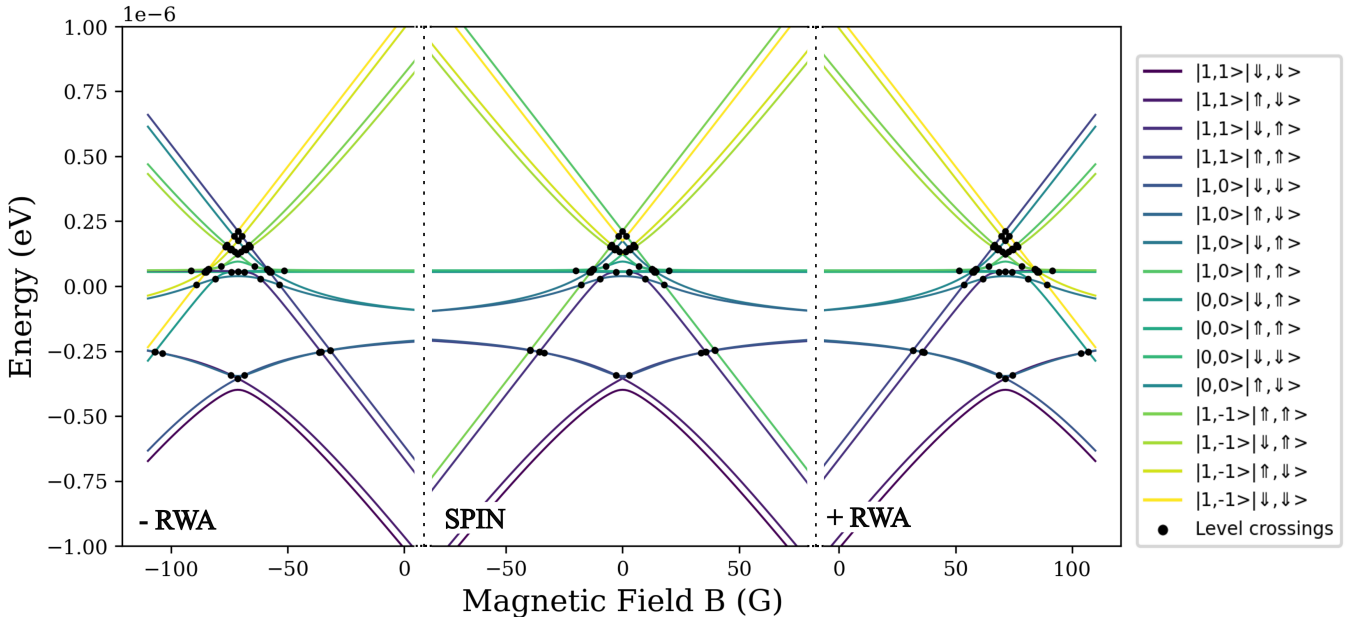


FIG. 1. Calculated eigen-energy spectra as a function of magnetic field B_0 . The middle panel shows the energy levels obtained from the pure static spin Hamiltonian \mathcal{H} of Equation 1, illustrating the zero-field manifold and linear Zeeman behavior. The left and right panels correspond to effective RWA Hamiltonians \mathcal{H}_{RWA} of Equation 5 with opposite detunings $\pm\Delta = \pm(\omega_0 - \omega)$, illustrating the symmetry of the driven level structure about $B_0 = 0$. Inclusion of the microwave drive produces additional resonance crossings near the resonance condition $g_e\mu_B|B_0| \approx \hbar\nu$ ($|B_0| \simeq 71.4$ G). Black markers indicate energy degeneracies where level crossings occur.

tion. We mimic this by central differencing the simulated current:

$$\frac{\partial I_{\text{sim}}(B_j; \theta)}{\partial B_0} \approx \frac{1}{B_{\text{mod}}} \left[I(B_j + \frac{1}{2}B_{\text{mod}}; \theta) - I(B_j - \frac{1}{2}B_{\text{mod}}; \theta) \right]. \quad (6)$$

The discrete derivative trace on the internal grid $\{B_j\}$ is then interpolated to the experimental field points $\{B_i\}$ using cubic splines. This requires two SLE solves per internal grid point (for the central difference) rather than one per experimental point, while keeping interpolation error negligible compared with experimental noise.

Given the interpolated simulation and measured data, we define the weighted residual

$$r_i(\theta) = w_i \left[\left(\frac{\partial I_{\text{sim}}}{\partial B_0} \right) (B_i; \theta) - \left(\frac{\partial I_{\text{exp}}}{\partial B_0} \right) (B_i) \right]. \quad (7)$$

We choose weights

$$w_i = \left| \frac{d^2 I_{\text{exp}}}{dB_0^2} (B_i) \right|, \quad (8)$$

computed from the measured derivative trace $\partial I_{\text{exp}}/\partial B_0$ by applying a Savitzky-Golay differentiating filter (derivative order 1) with window length 21 points, polynomial order 3, and sampling step $\Delta B_{\text{exp}} = 0.0400$ G.²⁶ This emphasizes sharp spectral structure and down-weights slowly varying background. The least-squares

objective is

$$\chi^2(\theta) = \sum_i r_i(\theta)^2, \quad (9)$$

which is minimized with respect to θ .

Nonlinear optimization of θ is performed with the trust-region reflective algorithm implemented in `scipy.optimize.least_squares`²¹, using box constraints derived from the priors. Box constraints were chosen as simple ranges around the prior values: for each coupling and rate, the allowed interval was taken to be [0.1, 10] times the corresponding initial magnitude, with g_e restricted to a narrow window about 2.00 and the dipolar parameters D_1 and D_2 constrained to remain within one order of magnitude of their prior values. The procedure yields a best-fit parameter set $\hat{\theta}$ that reproduces the full cw-EDMR sweep (Sec. III A). Low-field structure is analyzed separately by holding $\hat{\theta}$ fixed and varying D_2 as described in Sec. III B. The fitted values used for the global cw-EDMR fit in Sec. III A are collected in Table II.

The transverse dipolar parameter D_2 is only weakly constrained by the full-sweep data, because no half-field response is resolved above the noise floor in the experimental spectrum. In the global fit of Sec. III A we therefore impose a small prior on D_2 and find that the optimizer converges to a value $D_2 \approx 1.8 \times 10^{-11}$ eV (~ 4 kHz), for which the simulated half-field signal is negligible on the scale of the observed resonances. This choice improves the description of the features that are actually

resolved in the cw-EDMR sweep without artificially introducing a visible half-field line where none is observed.

III. RESULTS

A. Global fit to the cw-EDMR spectrum

The parameter set $\hat{\theta}$ obtained in Sec. II 5 reproduces the full continuous-wave (cw) EDMR sweep over the range $B_0 \in [-80, 80]$ G. We use an internal grid of $N_{\text{int}} = 200$ points, corresponding to a step size of $\Delta B = 0.8$ G. Numerical convergence was verified by doubling N_{int} , which changes the simulated derivative spectrum by $< 2\%$ in RMS of the derivative trace over $[-80, 80]$ G. This resolution is also comfortably finer than typical cw-EDMR peak-to-peak linewidths reported in related electrically detected resonance experiments (order 1-10 G).^{28,29} Figure 2 compares the simulated $\partial I_{\text{sim}} / \partial B_0(B_0; \hat{\theta})$ with a measured derivative signal $\partial I_{\text{exp}} / \partial B_0$. We collected this data using a 200 MHz RF signal, and the depicted spectrum does not have background subtraction applied. Additional experimental details are provided in the Supplementary Material.

The main panel shows agreement in the position and sign of the three dominant resonances: the central feature near $B_0 = 0$ and the high-field resonant pair near $\approx \pm 71.4$ G predicted by the driven spin Hamiltonian. The hyperfine-induced substructure "bumps" on the outer resonances are also well reproduced.³⁰ At the same time, several systematic differences remain. In the shoulders between the central feature and the outer resonances the simulated derivative is slightly offset: on the $B_0 > 0$ side the model overestimates the magnitude of the current, while on the $B_0 < 0$ side it underestimates it. In addition, the simulated zero-field line does not perfectly overlay the measured signal; the peak-to-peak amplitude of the central feature is somewhat smaller in the calculation than in the experiment.

The bottom panel shows the weighted residual $r_i(\hat{\theta})$ (Sec. II 5). The largest structured deviations occur on the flanks of the outer resonances and in the zero-field feature, and are confined to narrow field intervals. They mainly reflect modest amplitude/lineshape differences rather than missing or shifted resonances.

This full-sweep fit serves two purposes. First, it demonstrates that a single, physically constrained parameter set accounts for the main features of the cw-EDMR response without ad hoc, field-dependent adjustments. Second, it provides a consistent baseline for analyzing more subtle structure. In the following subsections we interpret fitted half-field resonances and other off-resonant features in greater detail.

B. Half-field and sub-half-field structure

Figure 3 magnifies the low-field window $B_0 \in [25, 40]$ G, where a weak half-field response is resolved near $B_0 \approx 32$ G. To probe the role of the transverse dipolar term, we vary D_2 about its small global-fit value while holding all other parameters fixed at $\hat{\theta}$. For the comparison in Fig. 3, we use $D_2^* = 2.0 \times 10^{-10}$ eV to match the observed half-field peak-to-peak scale in the low-field spectrum and denote the resulting parameter vector by $\theta(D_2^*)$. This choice also produces a weaker sub-half-field shoulder while remaining consistent with the absence of a clearly resolved half-field line in the full-sweep spectrum.

The simulation computed with $\theta(D_2^*)$ reproduces the overall asymmetry of the feature and a shoulder on its high-field side, but it underestimates the peak-to-peak amplitude and places the minimum at a slightly shifted field. These differences appear as a coherent, localized deviation of the residual in the half-field window, while the residual remains small outside this region (bottom panel of Fig. 3). The half-field response in this model arises from nominally "forbidden" $\Delta m_S = \pm 2$ transitions within the triplet manifold, enabled by the transverse part of the electron-electron dipolar interaction. In the coupled-electron basis $\{|s, m_s\rangle\}$, the effective two-electron dipolar Hamiltonian acts as

$$\begin{aligned} \hat{\mathcal{H}}_{DD,ee} |s, m_s\rangle &= D_1 m_s^2 |s, m_s\rangle - \frac{D_1}{3} s(s+1) |s, m_s\rangle \\ &+ \frac{D_2}{2} [s(s+1) - m_s(m_s+1)] |s, m_s+2\rangle \\ &+ \frac{D_2}{2} [s(s+1) - m_s(m_s-1)] |s, m_s-2\rangle, \end{aligned} \quad (10)$$

where D_1 is the axial dipolar parameter and D_2 is the transverse (crystal-field) parameter. The D_1 terms generate the familiar diagonal zero-field splitting of the triplet sublevels, whereas the terms proportional to D_2 couple $|m_s\rangle$ to $|m_s \pm 2\rangle$. These off-diagonal couplings mix the $m_s = \pm 1$ levels and allow double-quantum transitions at roughly half the main resonance field. In the limit $D_2 \rightarrow 0$ the $\Delta m_S = \pm 2$ matrix elements vanish and the half-field feature is suppressed.

Optical and ODMR studies of V_{Si}^- in 4H-SiC describe the $S = 3/2$ ground state by a nearly axial zero-field Hamiltonian, with a Kramers-doublet separation of about 70 MHz, corresponding to $D \approx 35$ MHz in the common 2D convention.³¹ Deviations from axial symmetry are typically parameterized by a transverse ZFS term (often denoted E) and are small enough that $E \simeq 0$ is a good approximation in the literature.³¹ In our effective pair model the half-field response is enabled by the transverse mixing term (parameterized by D_2), so a small transverse component naturally makes the half-field feature weak and sensitive to local strain, orientation, and crystal-field variations.

In our effective pair model, D_1 parameterizes the zero-field splitting of the defect-carrier triplet manifold rather

TABLE I. Initial parameter values used for nonlinear least-squares fitting. Energies are given in eV with MHz equivalents; magnetic fields are in Gauss and rates are in Hz.

Block	Parameter	Symbol	Value	MHz equiv.
Exchange ²⁵	Exchange coupling	J	4.1×10^{-9}	0.992
Hyperfine ^{23,24}	Hyperfine (Si on electron a)	A_{a1}	5×10^{-8}	12.1
	Hyperfine (Si on electron b)	A_{b1}	2.1×10^{-7}	50.8
	Hyperfine (C on electron a)	A_{a2}	3.3×10^{-8}	7.98
	Hyperfine (C on electron b)	A_{b2}	1.9×10^{-7}	45.9
Zeeman ^{24,27}	Electron g -factor	g_e	2.002	—
	Nuclear g -factor (²⁹ Si)	g_{n1}	-1.1106	—
	Nuclear g -factor (¹³ C)	g_{n2}	1.4048	—
ZFS / dipolar ^{13,24}	Dipolar parameter 1	D_1	1.5×10^{-7}	36.3
	Dipolar parameter 2	D_2	1.5×10^{-11}	3.63×10^{-3}
Microwave ^{28,29}	Drive frequency	ν	2.0×10^8	200
	Rabi frequency	ω_1	2.0×10^4 rad/s	$(\omega_1/2\pi) = 3.183 \times 10^3$
SLE kinetics ^{17,20}	Singlet recombination rate	k_S	10^5	—
	Dissociation rate	k_D	10^5	—
	Pair generation rate	p	10^2	—

TABLE II. Best-fit parameters obtained from the least-squares procedure described in Sec. II 5.

Block	Parameter	Symbol	Fitted Value	MHz equiv.
Exchange	Exchange coupling	J	3.44×10^{-9}	0.832
Hyperfine	Hyperfine (Si on electron a)	A_{a1}	5.438×10^{-8}	13.1
	Hyperfine (Si on electron b)	A_{b1}	4.658×10^{-7}	113
	Hyperfine (C on electron a)	A_{a2}	4.209×10^{-8}	10.2
	Hyperfine (C on electron b)	A_{b2}	9.242×10^{-8}	22.3
Zeeman	Electron g -factor	g_e	2.0008097169	—
	Nuclear g -factor (²⁹ Si)	g_{n1}	-1.110104	—
	Nuclear g -factor (¹³ C)	g_{n2}	1.4056972	—
ZFS / dipolar	Dipolar parameter 1	D_1	1.4863×10^{-7}	35.9
	Dipolar parameter 2	D_2	1.7528×10^{-11}	4.24×10^{-3}
Microwave	Drive frequency	ν	2.0×10^8	200
	Rabi frequency	ω_1	2.0×10^4 rad/s	$(\omega_1/2\pi) = 3.183 \times 10^3$
SLE kinetics	Singlet recombination rate	k_S	7.7337×10^4	—
	Dissociation rate	k_D	7.5563×10^4	—
	Pair generation rate	p	4.2477×10^2	—

than the intrinsic $S = 3/2$ fine structure of an isolated V_{Si}^- . Accordingly, the best-fit D_1 can differ from the canonical quartet value while still setting the relevant triplet splitting that governs SDR.

The global fit constrains D_1 through the overall triplet splitting, whereas D_2 is only weakly constrained by the main resonances. Small changes in D_2 therefore produce visible changes in the half-field response: within the range compatible with the full-sweep fit, increasing $|D_2|$ increases the half-field peak-to-peak amplitude and slightly shifts its apparent center field (Fig. 3).

Figure 4 shows the dependence of the simulated low-field response on D_2 with all other parameters held fixed.

As $|D_2|$ increases, the half-field feature near $B_0 \approx 32$ G grows approximately linearly in peak-to-peak amplitude. A weaker feature also appears near $B_0 \approx 28$ G (a “sub-half-field” shoulder), arising from the same dipolar-enabled $\Delta m_S = \pm 2$ mixing acting on hyperfine-mixed triplet states. For D_2 values compatible with the full-sweep fit, this sub-half-field signal remains close to the experimental noise floor.

Overall, the half-field window provides a sensitive but delicate constraint on D_2 . The model reproduces the existence and approximate location of the half-field response and its growth with $|D_2|$, but residual discrepancies in center field and peak-to-peak amplitude likely re-

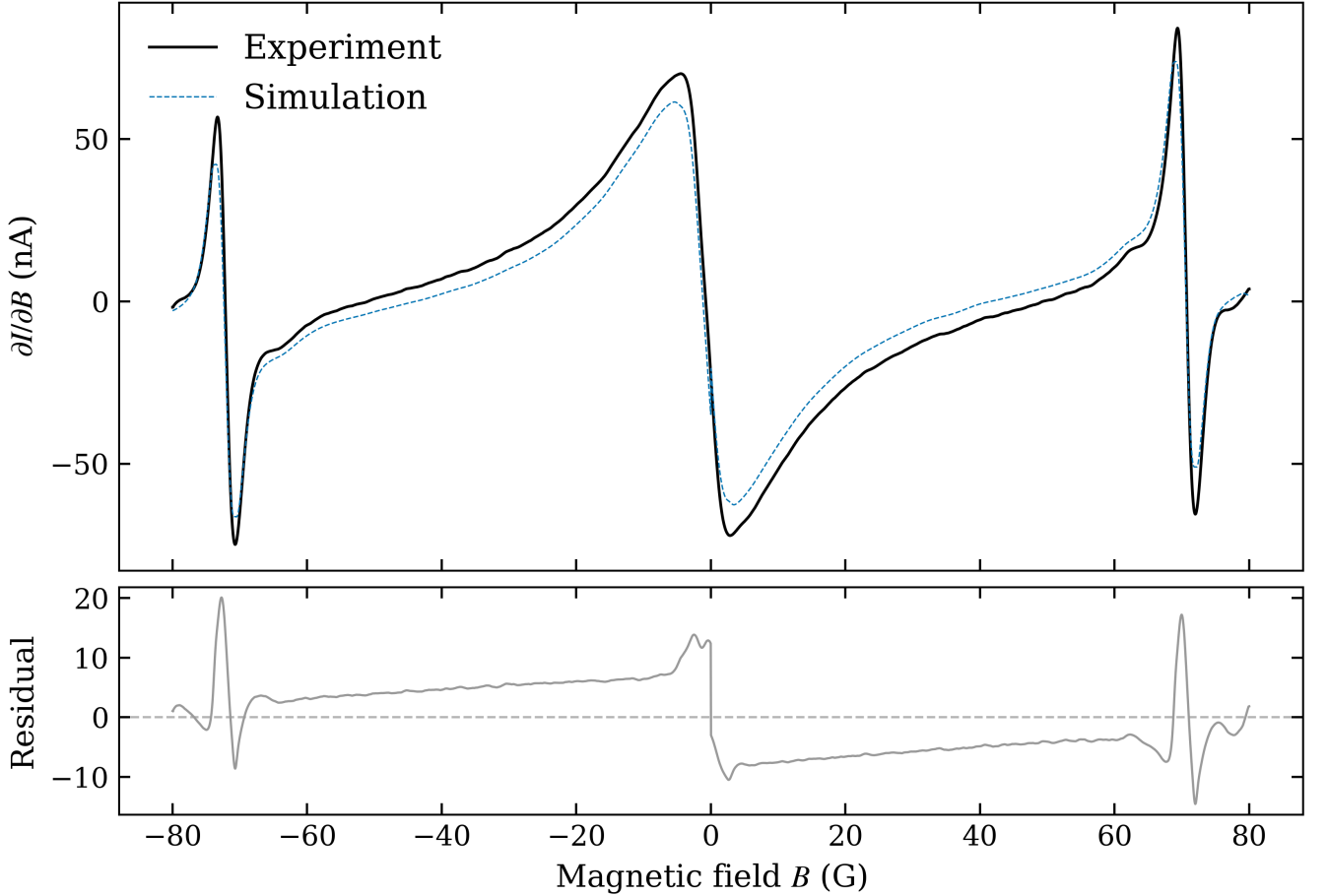


FIG. 2. Global fit of the cw-EDMR spectrum. Top: experimental lock-in derivative $\partial I_{\text{exp}} / \partial B_0$ (solid black) and simulation $\partial I_{\text{sim}} / \partial B_0(B_0; \hat{\theta})$ (dashed blue). Bottom: weighted residual $r_i(\hat{\theta})$ (Sec. II 5).

flect (i) the reduction of the effective dipolar/ZFS tensor to a minimal (D_1, D_2) form, (ii) neglected distributions of defect orientation and local strain, and (iii) uncertainty in the local microwave-field amplitude. Within these limitations, the data are consistent with a small but nonzero $D_2 \ll D_1$, as expected for V_{Si}^- in 4H-SiC.

C. Frequency-resolved simulations

The steady-state model can also be evaluated on a two-dimensional grid in static field B_0 and microwave frequency ν , yielding

$$\frac{\partial I_{\text{sim}}}{\partial B_0}(B_0, \nu; \theta(D_2^*)).$$

Figure 5 shows the resulting frequency-resolved spectrum.

In the overview [Fig. 5], the main resonance follows $g_e \mu_B |B_0| \approx h\nu$. Weaker structures appear at lower $|B_0|$, including the zero-field and half-field responses. A hor-

izontal cut at fixed ν recovers the corresponding one-dimensional cw-EDMR sweep.

The zoomed view in Fig. 5 focuses on the boxed high-field region. In addition to the main resonance, the simulation shows small off-resonant lobes that appear as ν is varied. Near $B_0 \approx 85$ G, pairs of such lobes track the resonance but are displaced from it in B_0 . A second family of paired features is visible near $B_0 \approx 55$ G, with a smaller separation in field.

A natural interpretation is that these paired features are hyperfine-assisted sidebands of the main electron-spin resonance. Finite hyperfine couplings shift the effective resonance condition between different nuclear manifolds, producing nearby loci in (B_0, ν) separated by $\Delta B \sim A/(g_e \mu_B)$ for characteristic hyperfine energies A . The simulated separations are of this order; a one-to-one assignment to specific nuclear manifolds is left for future work.

These frequency-resolved structures are predictions of the model rather than fit targets. The available dataset was acquired at a single drive frequency, and any off-resonant response near 85 G is marginal relative to the

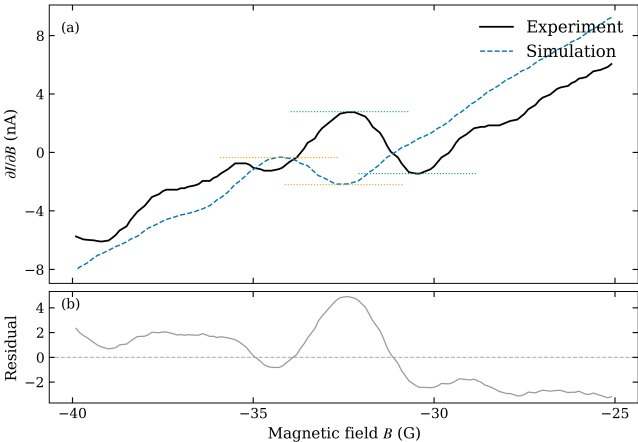


FIG. 3. Half-field region of the cw-EDMR spectrum. Top: experimental derivative $\partial I_{\text{exp}}/\partial B_0$ (solid black) and simulation $\partial I_{\text{sim}}/\partial B_0(B_0; \theta(D_2^*))$ (dashed blue) in the field window containing the half-field response. Bottom: corresponding weighted residual $r_i(\theta(D_2^*))$ (Sec. II 5).

noise. The 2D simulation therefore serves as a consistency check: the Hamiltonian and kinetics inferred from the cw sweep naturally generate additional off-resonant structure. A frequency-swept EDMR measurement would directly test the predicted paired features near 55 and 85 G.

IV. DISCUSSION

The steady-state SDR model reproduces the dominant cw-EDMR features of the V_{Si}^- -carrier ensemble using a single, physically constrained parameter set (Fig. 2). It captures (i) the sign and positions of the high-field resonant pair near $\pm B_{\text{res}}$, (ii) the overall shape of the near-zero-field response, and (iii) weak hyperfine-induced structure on the outer lines. Under our measurement conditions, this supports a picture in which the cw-EDMR sweep is governed primarily by microwave-driven singlet-triplet mixing within an effective two-electron manifold, as in standard SDR pair models.^{16–19} The structured residuals in Fig. 2 then delineate the specific field regions where additional ingredients are required.

A key outcome of the global fit is that the extracted interaction scales are consistent with a weakly coupled defect-carrier pair: a dominant axial dipolar/ZFS-like splitting in the triplet sector (captured by D_1), hyperfine couplings in the $\sim 10\text{-}10^2$ MHz range, and an exchange interaction J in the sub-MHz regime.^{16–18,25} The fitted hyperfine parameters fall within the order-of-magnitude range reported for nearby ^{29}Si and ^{13}C ligands of V_{Si}^- in ENDOR/ODMR studies.^{13,14,23,24} This supports attributing the resolved outer-line substructure to hyperfine-assisted shifts of the resonance condition across nuclear manifolds, rather than to an additional defect species.

That a single effective $S = 1/2$ Kramers-doublet model accounts for the cw spectrum suggests that, at $\nu = 200$ MHz and in the low-field window considered here, the EDMR response is dominated by transitions within one doublet together with pair-induced singlet-triplet mixing, rather than requiring explicit access to the full $S = 3/2$ quartet manifold.^{13–15}

The low-field analysis isolates the transverse dipolar parameter D_2 as the primary parameter controlling the half-field intensity (Fig. 4). In this Hamiltonian, the half-field response originates from nominally “forbidden” $\Delta m_S = \pm 2$ triplet-sector transitions enabled by off-diagonal transverse dipolar mixing (Eq. 10). The weakness of the measured half-field line is therefore consistent with a largely axial effective interaction tensor and with ensemble averaging (e.g., orientation/strain distributions) that suppresses coherent transverse mixing. In related electrically detected resonance contexts, half-field responses and their coherent signatures have been used as sensitive probes of dipolar coupling and internal mixing within multi-spin complexes.³² Accordingly, the half-field window complements the full-sweep fit: although it is only weakly constrained by the dominant resonances, it is highly diagnostic of transverse coupling once the baseline Hamiltonian and kinetics are fixed. The remaining mismatch in center field and amplitude (Fig. 3) therefore points directly to approximations that most affect small, symmetry-sensitive lines: the reduction to a minimal (D_1, D_2) form, neglected distributions of pair orientation and local strain, and uncertainty in the effective microwave field at the defect site.

The 2D (B_0, ν) simulations provide an additional, testable prediction: the appearance of paired off-resonant features displaced from the main resonance in field (Fig. 5). A natural interpretation is that these lobes are hyperfine-assisted sidebands, reflecting slightly different resonance conditions across nuclear manifolds when the electron transition is dressed by finite hyperfine couplings of the magnitude reported for V_{Si}^- ligands.^{23,24} Such structure is not a fit target in the present dataset, but it is precisely the type of feature that becomes accessible in frequency-agile EDMR platforms. Recent efforts toward more compact and frequency-flexible EDMR implementations make direct tests of this kind feasible.³³ A multi-frequency cw-EDMR measurement would therefore serve two purposes: it would validate whether the predicted sidebands are realized experimentally, and it would help disambiguate which subset of hyperfine parameters is actually constrained by a single-frequency sweep versus inherited from priors.

Several extensions would strengthen the physical interpretability of the fitted parameters and address the systematic discrepancies visible in Fig. 2. First, the effective $S = 1/2$ reduction can be relaxed by explicitly modeling the $S = 3/2$ ground-state manifold of V_{Si}^- together with its intrinsic fine structure and small transverse terms.^{13–15} This would place the cw spectrum, half-field response, and near-zero-field structure within a sim-

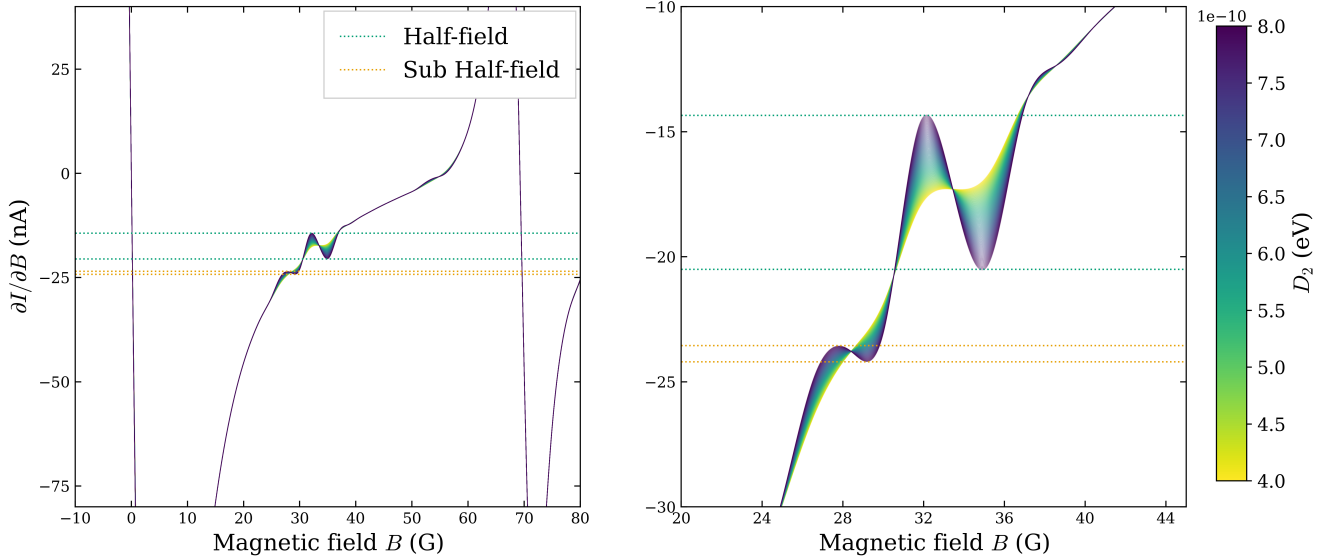


FIG. 4. Dependence of the simulated half-field response on the transverse dipolar (crystal-field) parameter D_2 . Left: overview of the simulated cw-EDMR spectrum showing the low-field region where the half-field and sub-half-field features appear. Right: zoom of the 25–40 G window; each trace corresponds to a different D_2 , color-coded by its magnitude. Increasing $|D_2|$ enhances both the main half-field feature near $B_0 \approx 32$ G and the weaker sub-half-field structure near $B_0 \approx 28$ G.

gle microscopic Hamiltonian rather than mapping quartet physics onto an effective triplet splitting in the pair sector.

Second, the isotropic-contact hyperfine approximation can be replaced by anisotropic tensors and a small set of candidate nuclear configurations, enabling more direct assignment of the observed outer-line substructure and more quantitative predictions of hyperfine sidebands.^{23,24}

Third, the kinetic model can be generalized beyond a single singlet-selective recombination pathway by including additional relaxation channels and/or state-dependent capture and dissociation processes, as in broader SDR frameworks.^{16,17} In cw-EDMR, the detected quadrature, modulation parameters, and the balance of recombination, dissociation, and relaxation can reshape lineshapes and can alter the apparent sign of resonances; systematic sweeps of modulation frequency and microwave power therefore provide a direct route to separating kinetic from Hamiltonian effects.³⁴ Experimentally, measuring the lock-in phase response (in-phase and quadrature) as a function of B_{mod} and modulation frequency would add independent constraints on (k_S, k_D, p) and on any missing relaxation channels.³⁴

Finally, time-domain measurements provide an orthogonal path forward. Pulsed EDMR can isolate spin-dependent processes, identify paramagnetic partners, and extract couplings from coherent dynamics and echo-based methods, particularly in multi-channel recombination environments.³⁵ Here, pEDMR would be valuable for (i) distinguishing whether the central-feature mismatch reflects an additional recombination channel versus inhomogeneous broadening and saturation, and (ii) directly constraining the transverse mixing responsible for the

half-field response through its coherent signatures. Together, these extensions would move the present cw description toward a quantitatively predictive model that links spectral features to specific microscopic couplings and recombination pathways in SiC devices.

V. CONCLUSION

We presented a steady-state simulation framework for cw-EDMR spectra of V_{Si}^- -associated spin-dependent recombination in 4H-SiC, combining an effective defect-carrier pair Hamiltonian with singlet-selective kinetics in a stochastic Liouville formalism. Solving the driven steady state as a Sylvester equation enables efficient field-swept spectrum evaluation and least-squares parameter estimation without explicit time propagation. A single fitted parameter set reproduces the dominant features of the measured cw sweep, including the high-field resonant pair and resolved hyperfine-induced structure. By isolating the transverse dipolar term, the model explains the emergence and scaling of weak half-field and sub-half-field responses as dipolar-enabled double-quantum mixing in the triplet sector. Frequency-resolved simulations further predict off-resonant sidebands that provide concrete targets for multi-frequency EDMR measurements. Together, these results show that steady-state Liouville simulations offer a physically transparent and computationally tractable route to quantitative interpretation of EDMR spectra in SiC defect systems and related semiconductor platforms.

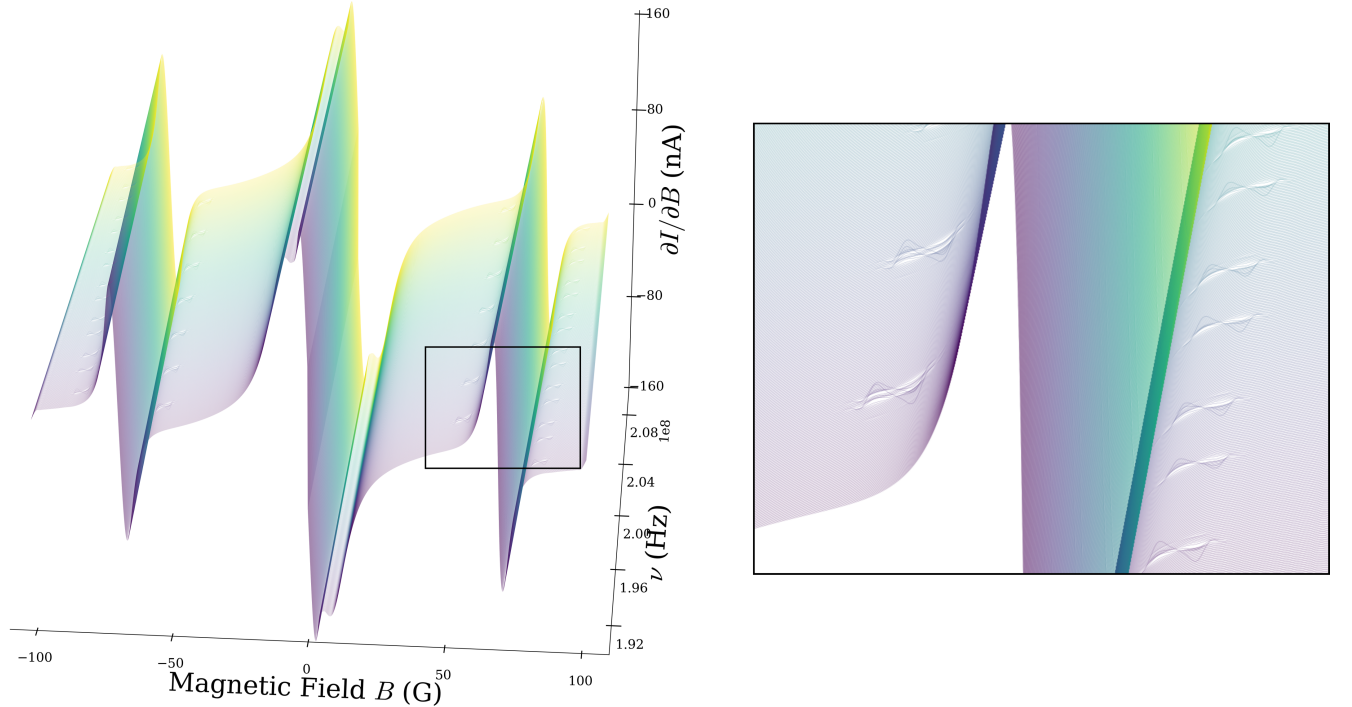


FIG. 5. Simulated frequency-resolved cw-EDMR spectrum computed with $\theta(D_2^*)$. Left: $\partial I_{\text{sim}}/\partial B_0(B_0, \nu; \theta(D_2^*))$ versus B_0 and ν . Right: zoom of the boxed region highlighting paired off-resonant features near $B_0 \approx 85$ G and $B_0 \approx 55$ G.

SUPPLEMENTARY MATERIAL

See the Supplementary Material for additional experimental details on the RF excitation and field-modulation scheme and on the data acquisition and processing procedures, as well as a derivation and implementation details of the Spin Hamiltonian in Eq. (1).

ACKNOWLEDGMENTS

This work was majority supported by NASA Glenn Research Center's Science Mission Directorate (SMD) and partially based on work supported by the U.S. Department of Energy, Office of Science, Office of Advanced Scientific Computing Research (ASCR), Reaching a New Energy Sciences Workforce (RENEW) under award number DE-SC0024219. We would also like to thank Drs. Jesse Berevosky and Gary Hunter for their content discussions and suggestions.

AUTHOR DECLARATIONS

Conflict of Interest

The authors have no conflicts to disclose.

Author Contributions

Deval Deliwala: Conceptualization (equal); Formal analysis (lead); Investigation (equal); Methodology (equal); Software (lead); Visualization (lead); Writing-original draft (lead); Writing-review & editing (equal).

Ryan Byrne: Conceptualization (equal); Data curation (lead); Formal analysis (equal); Investigation (equal); Methodology (supporting); Validation (lead); Writing-original draft (equal); Writing-review & editing (equal).

Daniel Hart: Conceptualization (lead); Data curation (supporting); Formal analysis (supporting); Funding acquisition (lead); Investigation (equal); Methodology (equal); Project administration (lead); Resources (lead); Software (supporting); Supervision (lead); Writing-original draft (equal); Writing-review & editing (equal).

DATA AVAILABILITY

The data that support the findings of this study are available from the corresponding author upon reasonable request.

REFERENCES

- ¹P. M. Lenahan and J. F. Conley, Jr., *Journal of Vacuum Science & Technology B* **16**, 2134 (1998).
- ²J. J. L. Morton and B. W. Lovett, *Annual Review of Condensed Matter Physics* **2**, 189 (2011).
- ³C. J. Cochran, P. M. Lenahan, and A. J. Lelis, *Journal of Applied Physics* **109**, 014506 (2011).
- ⁴D. J. Christle, A. L. Falk, P. Andrich, P. V. Klimov, J. U. Hassan, N. T. Son, E. Janzén, T. Ohshima, and D. D. Awschalom, *Nature Materials* **14**, 160 (2015).
- ⁵R. Nagy, M. Niethammer, M. Widmann, Y.-C. Chen, P. Udvarhelyi, C. Bonato, J. U. Hassan, R. Karhu, I. G. Ivanov, N. T. Son, J. R. Maze, T. Ohshima, Ö. O. Soykal, Á. Gali, S.-Y. Lee, F. Kaiser, and J. Wrachtrup, *Nature Communications* **10**, 1954 (2019).
- ⁶A. L. Falk, P. V. Klimov, V. Ivády, K. Szász, D. J. Christle, W. F. Koehl, Á. Gali, and D. D. Awschalom, *Physical Review Letters* **114**, 247603 (2015).
- ⁷V. A. Soltamov, B. V. Yavkin, G. V. Mamin, S. B. Orlinskii, I. D. Breev, A. P. Bundakova, R. A. Babunts, A. N. Anisimov, and P. G. Baranov, *Physical Review B* **104**, 125205 (2021).
- ⁸K. Fukui, T. Sato, H. Yokoyama, H. Ohya, and H. Kamada, *Journal of Magnetic Resonance* **149**, 13 (2001).
- ⁹C. Boehme and K. Lips, *Physical Review B* **68**, 245105 (2003).
- ¹⁰C. Boehme and K. Lips, *Applied Magnetic Resonance* **27**, 109 (2004).
- ¹¹D. R. McCamey, G. W. Morley, H. A. Seipel, L. C. Brunel, J. van Tol, and C. Boehme, *Physical Review B* **78**, 045303 (2008).
- ¹²S. G. Carter, A. Shabaev, S. E. Economou, T. A. Kennedy, A. S. Bracker, and T. L. Reinecke, *Physical Review Letters* **102**, 167403 (2009).
- ¹³D. Simin, V. A. Soltamov, A. V. Poshakinskiy, A. N. Anisimov, R. A. Babunts, D. Tolmachev, E. N. Mokhov, M. Trupke, S. A. Tarasenko, P. G. Baranov, and V. Dyakonov, *Physical Review X* **6**, 031014 (2016).
- ¹⁴M. Niethammer, M. Widmann, S.-Y. Lee, P. Stenberg, O. Kordina, T. Ohshima, N. T. Son, E. Janzén, and J. Wrachtrup, *Physical Review Applied* **6**, 034001 (2016).
- ¹⁵S. A. Tarasenko, A. V. Poshakinskiy, D. Simin, V. A. Soltamov, E. N. Mokhov, P. G. Baranov, V. Dyakonov, and G. V. Astakhov, *Physica Status Solidi (b)* **255**, 1700258 (2018).
- ¹⁶D. Kaplan, I. Solomon, and N. F. Mott, *Journal de Physique Lettres* **39**, L51 (1978).
- ¹⁷C. Boehme and K. Lips, *Physical Review B* **68**, 245105 (2003).
- ¹⁸D. R. McCamey, G. W. Morley, H. Seipel, L.-C. Brunel, J. van Tol, and C. Boehme, *Physical Review B* **78**, 045303 (2008).
- ¹⁹M. E. Limes, J. Wang, W. J. Baker, S.-Y. Lee, B. Saam, and C. Boehme, *Physical Review B* **87**, 165204 (2013).
- ²⁰T. Hansen and N. L. Pedersen, *Chemical Physics Letters* **363**, 636 (2002).
- ²¹P. Virtanen, R. Gommers, T. E. Oliphant, M. Haberland, T. Reddy, D. Cournapeau, E. Burovski, P. Peterson, W. Weckesser, J. Bright, S. J. van der Walt, M. Brett, J. Wilson, K. J. Millman, N. Mayorov, A. R. J. Nelson, E. Jones, R. Kern, E. Larson, C. J. Carey, Í. Polat, Y. Feng, E. W. Moore, J. VanderPlas, D. Laxalde, J. Perktold, R. Cimrman, I. Henriksen, E. A. Quintero, C. R. Harris, A. M. Archibald, A. H. Ribeiro, F. Pedregosa, P. van Mulbregt, and SciPy 1.0 Contributors, *Nature Methods* **17**, 261 (2020).
- ²²E. Sörman, N. T. Son, W. M. Chen, O. Kordina, C. Hallin, and E. Janzén, *Physical Review B* **61**, 2613 (2000).
- ²³N. T. Son, P. Stenberg, V. Jokubavicius, T. Ohshima, J. U. Hassan, and I. G. Ivanov, *Journal of Physics: Condensed Matter* **31**, 195501 (2019).
- ²⁴V. A. Soltamov, B. V. Yavkin, G. V. Mamin, S. B. Orlinskii, I. D. Breev, A. P. Bundakova, R. A. Babunts, A. N. Anisimov, and P. G. Baranov, *Physical Review B* **104**, 125205 (2021).
- ²⁵K.-i. Fukui, T. Umeda, K.-i. Ishibashi, and M. Ohishi, *Journal of Magnetic Resonance* **149**, 13 (2001).
- ²⁶A. Savitzky and M. J. E. Golay, *Analytical Chemistry* **36**, 1627 (1964).
- ²⁷N. J. Stone, *Atomic Data and Nuclear Data Tables* **90**, 75 (2005).
- ²⁸M. Eckardt, J. Behrends, D. Münter, and W. Harneit, *AIP Advances* **5**, 047139 (2015).
- ²⁹J. Lu, F. Hoehne, A. R. Stegner, L. Dreher, M. Stutzmann, M. S. Brandt, and H. Huebl, *Physical Review B* **83**, 235201 (2011).
- ³⁰C. T.-K. Lew, *All-electrical Quantum Sensing with Silicon Carbide Devices*, Ph.d. thesis, University of Melbourne, Melbourne, Australia (2022).
- ³¹D. Simin, A. Sperlich, G. V. Astakhov, A. V. Poshakinskiy, V. A. Soltamov, S. A. Tarasenko, P. G. Baranov, and V. Dyakonov, *Physical Review Applied* **4**, 014009 (2015), arXiv:1505.00176.
- ³²W. J. Baker, T. L. Keevers, C. Boehme, and D. R. McCamey, “Using coherent dynamics to quantify spin-coupling within triplet-exciton/polaron complexes in organic diodes,” (2015), arXiv:1502.05471.
- ³³J. Lettens, M. Avramenko, I. Vandevenne, A. Chu, P. Hengel, M. Kern, J. Anders, P. Moens, E. Goovaerts, and S. Cambré, *Journal of Applied Physics* **137**, 065705 (2025).
- ³⁴S.-Y. Lee, C. Boehme, and D. R. McCamey, *Physical Review B* **86**, 115204 (2012), arXiv:1208.5573.
- ³⁵A. Schnegg, J. Behrends, M. Fehr, K. Lips, and C. Boehme, *Physical Chemistry Chemical Physics* **14**, 14418 (2012).